Advances in Materials Research, *Vol. 14, No. 5 (2025) 397-416*
https://doi.org/10.12989/amr.2025.14.5.397

Management of dynamic stability in Cu-Ni carbon composite structures via physics-informed neural network modeling

Anber Abraheem Shlash Mohammad[1], Suleiman Ibrahim Mohammad*[2,3],
Badrea Al Oraini[4], Sultan Alaswad Alenazi[5] and Asokan Vasudevan[6,7]

[1]Digital Marketing Department, Faculty of Administrative and Financial Sciences, University of Petra, Jordan
[2]Electronic Marketing and Social Media, Economic and Administrative Sciences Zarqa University, Jordan
[3]Research follower, INTI International University, 71800 Negeri Sembilan, Malaysia
[4]Department of Business Administration, Collage of Business and Economics, Qassim University
[5]Marketing Department, College of Business, King Saud University, Riyadh 11362, Saudi Arabia
[6]Faculty of Business and Communications, INTI International University, 71800 Negeri Sembilan, Malaysia
[7]Shinawatra University, 99 Moo 10, Bangtoey, Samkhok, Pathum Thani 12160 Thailand

(*Received July 30, 2025, Revised August 28, 2025, Accepted August 28, 2025*)

Abstract. Dynamic stability management within multifunctional composite systems is vital for the development and structural reliability of engineering applications. The study focuses on Cu–Ni carbon composite structure management with an integrated framework of micromechanical modeling, higher-order shear deformation theory, and physics-informed neural networks (PINNs). Effective material properties are modeled by modified Halpin–Tsai models, allowing improved management of constituent interactions between Cu–Ni matrix and the carbon reinforcements. The equations of motion are formulated in accordance with Hamilton's principle and Hooke's law, establishing and maintaining a consistent variational formulation with three independent components for displacement. It is recognized that as substructural interactions are more effectively managed, the elastic foundation can consist of Winkler's and Pasternak's coefficients, incorporating both normal and shear-layer contributions. Higher-order shear deformation theory is applied to properly characterize the stress–strain state during representation, eliminating the need for shear correction factors, permitting better predictive management of moderately thick plates. A PINN-based solution procedure is developed in which the governing partial-differential equations, along with the boundary values called upon during learning, are embedded within the learning process. The machine learning framework allows efficient use of resources with the potential for more robust accuracy in predicting stability boundaries, critical buckling loads, and vibration responses. The comparison studies show that the proposed procedure offers advantages over an existing and historical finite element model. The results of the studies also illustrated that PINNs offered more effective predictive management of composite dynamic stability and represented a hybrid of material modeling, structural theory, and machine learning. Hence, this work contributes to the continuing advancements of materials development by providing a promising platform for the next generation of multi-functional composites.

Keywords: Cu–Ni carbon composite; dynamic stability management; higher-order shear deformation theory; modified Halpin–Tsai model; physics-informed neural networks

---

*Corresponding author, Ph.D., E-mail: dr_sliman@yahoo.com

Copyright © 2025 Techno-Press, Ltd.
http://www.techno-press.org/?journal=amr&subpage=5 ISSN: 2234-0912 (Print), 2234-179X (Online)

1. Introduction

Composite materials are important in modern engineering since they give engineers the ability to exploit the strengths of two or more dissimilar materials and create properties that are greater than the individual parts (Zhai *et al*. 2025). The nature of composite materials provides a higher strength-to-weight ratio, which is important in structural engineering applications like aerospace, automotive, and building (Liu *et al*. 2025). Engineers appreciate composite materials because they are predominantly non-corrosive, which leads to a longer life in products within severe environments (Luo *et al*. 2025). Composite materials can be designed in ways that focus on the structural properties or performance, where engineers can orient fibers in any desired direction and choose what type of matrix to use (thermoset, thermoplastic, etc.) (Zerrouki *et al*. 2020). Furthermore, engineers also see some advantages in terms of their fatigue resistance. It is routine for engineers to design products that require a long operational or service life (Azmi *et al*. 2019). Composite materials provide engineers the ability to design obstacles that are lighter than metals yet maintain suitable strength and durability (Jayakumari *et al*. 2024). Composites can be associated with multiple thermal and electrical properties, making them attractive for items that require thermal insulation and/or electrical conductivity (Ebrahimi *et al*. 2019 a). Composite materials offer multiple and varied molding or additive methods to manufacture an object, which provide flexibility to mold complex shapes and for efficient production method (Ebrahimi *et al*. 2019 b). Composite materials have had a measurable impact on sustainability by reducing fuel and overall consumption in transportation, and also act as alternative supports for renewable technologies, such as wind turbine blades (Hajmohammad *et al*. 2018). In conclusion, composite materials offer many distinct options for better utility, performance, and foster the new age in industry and technology to adapt and flourish at a higher rate of pace (Madenci *et al*. 2023).

Stability analysis is important in engineering because it allows assurance that structures or systems can endure applied loads without collapsing or failing (Abderezak *et al*. 2018). Stability analysis gives engineers a degree of confidence regarding the outcome of a given situation, should the load be varied in different ways (i.e., external forces, oscillation, environmental conditions, etc.) on a system (Duc *et al*. 2025). Studying stability provides information about the locations of critical points that cause structural instability, or a sudden failure point (Garg *et al*. 2024). Therefore, stability is of utmost importance in the safety-engineering field for building, bridges, airplanes, and machinery (Zouatnia *et al*. 2019). Stability analysis is a means of avoiding costly accidents and maximizing the dependability of the engineering project (Tyona 2013). Stability analysis also affords the opportunity to optimize designs; thus, designs not only must be safe (stability is a critical aspect of safety), but they must also be economically justifiable, in terms of the materials used and the costs incurred (Rahimi *et al*. 2020). Stability considerations are every bit as important to the field of dynamic systems, or control engineering, in which small perturbations to systems lead to instability if not controlled or effectively managed (Safarpour *et al*. 2021). In engineering applications/considerations, engineers use stability analysis to evaluate static and dynamic responses, from buckling in columns to oscillation in mechanical systems (Wang *et al*. 2024). Stability is the basis for the development of a scientific rationale for codes and standards in engineering practice (Zhang *et al*. 2020). Stability is one of the most fundamentally used tools that helps engineers to create long-lasting, safe, and economical designs for practical designs (Rashvand *et al*. 2022).

Machine learning algorithms are significant because they allow computers to establish a model based on their experience using data, enabling them to make decisions without human intervention (Rabczuk *et al*. 2004). Machine learning algorithms are an essential tool for engineers and scientists, assisting them in solving problems that cannot easily be modeled mathematically (Talebi *et al.* 2014). An additional benefit of machine learning algorithms is that they can reduce resources needed to improve accuracy in areas like natural language processing, predictive analytics, or systems like image recognition (Samaniego *et al.* 2020). These algorithms are found in a variety of settings, including, but not limited to, healthcare, finance, and manufacturing. As machine learning algorithms are applied to data, they detect patterns and make predictions about future information based upon the knowledge within the dataset and the algorithms, which may be exploited for further explorations, forecasting findings, etc (Eshaghi *et al.* 2025). Machine learning algorithms can take in data and maintain or increase their accuracy over time (Guo *et al.* 2025). The capability to learn at an adaptable pace means machine learning algorithms should be utilized in any scenario that includes big data or other situations where 'change' occurs frequently or 'loudly' and definite conclusions are difficult to reach (Guo *et al.* 2023). Overall, machine learning algorithms act as instruments of evolution and innovation in technology businesses while giving credence and validity to more intelligent, capable decision-making (Liu *et al.* 2024).

Managing dynamic stability in Cu-Ni carbon composite structures involves the implementation of advanced modelling techniques that integrate micromechanical, structural, and computational fields of knowledge. The first step in this study was to use modified Halpin-Tsai models to obtain effective material properties for Cu-Ni carbon composites; the development of micromechanical descriptions allowed for accurate representations of reinforcement and interface effects. The governing equations describing motion were developed using Hooke's rule with Hamilton's principle to develop an association, and a higher-order shear deformation theory was employed with three displacement components to represent transverse shear without relying on empirical corrections. The elastic foundation was modelled with Winkler and Pasternak coefficients to enable realistic subgrade interactions, and this results in more accurate structural predictions when subjected to dynamic stresses. The proposed framework makes use of the physics-informed neural networks (PINN) as the primary solution procedure. Methods such as the PINNs utilize loss functions that embed physics and boundary conditions into their loss function to produce mesh-free, data-driven simulations. The resulting well-timed comparisons with classical finite element methods provided clear evidence of the effectiveness and computational efficiency of the PINN-based decision-making procedures. The results obtained regarding predicted vibration frequencies, buckling loads, and stability areas of composites improved, thus showing the effectiveness of the integrated framework for managing multifunctional composites in an engineering context.

The research reveals that physics-informed learning, advanced shear deformation theory, and homogenization methods may improve structural performance management in material research to perform better-informed allocations of resources. The major contributions of this work are: 1. enhanced Halpin–Tsai-style homogenization for Cu–Ni carbon composites with advanced shear deformation theory; 2. Hamilton's principle, elastic foundation (Winkler–Pasternak) modeling within a PINN-based system; and 3. a management-centric solution approach that combines physics-informed learning with dynamic stability analysis.

2. Theory and formulation

In this section, the governing equations have been manipulated into a format amenable to numerical implementation, where displacement, stress, and strain fields have been articulated in generalized coordinates. The effective elastic constants of the Cu–Ni carbon composite were

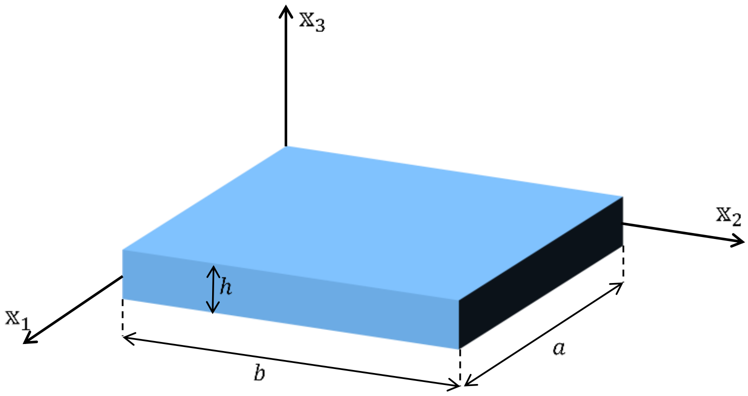

Fig. 1 A geometry of the presented plate made of Cu–Ni carbon composite material

embedded using modified Halpin–Tsai models, which produced efficient and accurate homogenization of the heterogeneous microstructure. A variationally consistent formulation has been developed to represent both bending and shear deformations, which expands the compliance of the model to moderately thick plates. The coupling of higher-order shear deformation theory and the elastic foundation model assures that composite systems fully capture the interaction between the composite structure and supporting medium. Depictions of the geometry of the plate represented in Cu–Ni carbon composite material are in Fig. 1.

2.1. Properties of composite media

2.1.1 Volume fraction of coarse aggregate (CA)

Through the thickness ($\mathbb{x}_3$), the reinforcement volume fraction ($\mathbb{x}_3$) may exhibit uniform (UD) or functionally graded (FG) distributions.

$$\begin{aligned} &\text{Pattern UD: } V_C(\mathbb{x}_3) = V_C^*, \\ &\text{Pattern O: } V_C(\mathbb{x}_3) = 2\left(1 - \frac{2|\mathbb{x}_3|}{h}\right) V_C^*, \\ &\text{Pattern X: } V_C(\mathbb{x}_3) = 4\left(\frac{|\mathbb{x}_3|}{h}\right) V_C^*, \\ &\text{Pattern A: } V_C(\mathbb{x}_3) = \left(1 - \frac{2\mathbb{x}_3}{h}\right) V_C^*, \end{aligned} \tag{1}$$

where the maximum volume percent of reinforcement, V_C^*, is determined by:

$$V_C^* = \frac{W_C}{W_C + (\frac{\rho^C}{\rho^m}) - (\frac{\rho^C}{\rho^m}) W_C} \tag{2}$$

where ρ^m and ρ^C represent the Cu–Ni matrix and carbon reinforcement, respectively, and W_C represents the carbon mass percentage.

2.1.2 Effective material properties of Cu–Ni Carbon Composite

Using modified Halpin-Tsai models and the law of mixtures, composite qualities are produced:

Table 1 Tested beams details

Property	Carbon Reinforcement	Cu–Ni Matrix
Elastic Modulus E_{11} (GPa)	600	170
Elastic Modulus E_{22} (GPa)	600	170
Shear Modulus G_{12} (GPa)	200	80
Poisson's Ratio ν_{12}	0.15	0.30
Density ρ (kg/m^3)	2,200	8,900

$$\begin{gathered}
E_{11} = \eta_1 V_{CA} E_{11}^C + V_m E^m,\ \frac{\eta_2}{E_{22}} = \frac{V_C}{E_{22}^C} + \frac{V_m}{E^m},\ \frac{\eta_3}{G_{12}} = \frac{V_C}{G_{12}^C} + \frac{V_m}{G^m}, \\
G_{12}^C = {E_{11}^C}\big/{2(1+\nu_C)},\ G^m = \frac{E^m}{2(1+\nu_m)}, \\
\nu_{12} = \nu_{CA} V_C + \nu_m V_m,\ \nu_{21} = \frac{\nu_{12} E_{22}}{E_{11}},\ \rho = \rho_{CA} V_C + \rho_m V_m \\
E_{33} = E_{22},\ G_{12} = G_{13} = G_{23},\ \nu_{13} = \nu_{12}, \nu_{31} = \nu_{21},\ \nu_{32} = \nu_{23} = \nu_{21},
\end{gathered} \tag{3}$$

The effective elastic moduli are represented by E_{11} and E_{22}, the shear modulus by G_{12}, Poisson's ratios by ν_{12} and ν_{21}, and mass density by ρ. The formula $V_m = 1 - V_C$ will be used to calculate the matrix's volume fraction. Moreover, size effects and the contribution of load applied to nanotubes and polymeric phases are connected to the efficiency metric $\eta_j (j = 1,2,3)$. The material characteristics of the building are shown in Table 1.

3. Mathematical model derivation

It is possible to describe the three displacement components $\mathbb{U}_1$, $\mathbb{U}_2$ and $\mathbb{U}_3$ as follows (Carrera 1996, 2001):

$$\mathbb{u}_1(\mathbb{x}_1, \mathbb{x}_2, \mathbb{x}_3, t) = \mathfrak{U}_0(\mathbb{x}_1, \mathbb{x}_2, t) + \mathbb{x}_3 \mathfrak{U}_1(\mathbb{x}_1, \mathbb{x}_2, t) + \mathbb{x}_3^3 \mathfrak{U}_3(\mathbb{x}_1, \mathbb{x}_2, t), \tag{4a}$$

$$\mathbb{u}_2(\mathbb{x}_1, \mathbb{x}_2, \mathbb{x}_3, t) = \mathfrak{V}_0(\mathbb{x}_1, \mathbb{x}_2, t) + \mathbb{x}_3 \mathfrak{V}_1(\mathbb{x}_1, \mathbb{x}_2, t) + \mathbb{x}_3^3 \mathfrak{V}_3(\mathbb{x}_1, \mathbb{x}_2, t), \tag{4b}$$

$$\mathbb{u}_3(\mathbb{x}_1, \mathbb{x}_2, \mathbb{x}_3, t) = \mathfrak{W}_0(\mathbb{x}_1, \mathbb{x}_2, t) + \mathbb{x}_3 \mathfrak{W}_1(\mathbb{x}_1, \mathbb{x}_2, t) + \mathbb{x}_3^2 \mathfrak{W}_2(\mathbb{x}_1, \mathbb{x}_2, t). \tag{4c}$$

where $\mathbb{u}_1$, $\mathbb{u}_2$, and $\mathbb{u}_3$ are the displacements in the $\mathbb{x}_1$-, $\mathbb{x}_2$-, and $\mathbb{x}_3$-directions, respectively. $\mathfrak{U}_0$, $\mathfrak{U}_1$, $\mathfrak{U}_3$, $\mathfrak{V}_0$, $\mathfrak{V}_1$, $\mathfrak{V}_3$, $\mathfrak{W}_0$, $\mathfrak{W}_1$, and $\mathfrak{W}_2$ are functions to be determined. The constitutive equations of Eq. (5) are given by:

$$\begin{Bmatrix} \mathcal{E}_{11} \\ \mathcal{E}_{22} \\ \gamma_{12} \end{Bmatrix} = \begin{Bmatrix} \mathcal{E}_{11}^0 \\ \mathcal{E}_{22}^0 \\ \gamma_{12}^0 \end{Bmatrix} + \mathbb{x}_3 \begin{Bmatrix} \mathcal{E}_{11}^1 \\ \mathcal{E}_{22}^1 \\ \gamma_{12}^1 \end{Bmatrix} + \mathbb{x}_3^3 \begin{Bmatrix} \mathcal{E}_{11}^2 \\ \mathcal{E}_{22}^2 \\ \gamma_{12}^2 \end{Bmatrix}, \tag{5a}$$

$$\begin{Bmatrix} \gamma_{23} \\ \gamma_{13} \end{Bmatrix} = \begin{Bmatrix} \gamma_{23}^0 \\ \gamma_{13}^0 \end{Bmatrix} + \mathbb{x}_3 \begin{Bmatrix} \gamma_{23}^1 \\ \gamma_{13}^1 \end{Bmatrix} + \mathbb{x}_3^2 \begin{Bmatrix} \gamma_{23}^2 \\ \gamma_{13}^2 \end{Bmatrix}, \tag{5b}$$

$$\mathcal{E}_{33} = \mathcal{E}_{33}^1 + 2\mathbb{x}_3 \mathcal{E}_{33}^2. \tag{5c}$$

the first derivative concerning $\mathbb{x}_3$ and

$$\mathcal{E}_{11}^{0}=\frac{\partial\mathfrak{U}_0}{\partial\mathbb{x}_1},\ \mathcal{E}_{11}^{1}=\frac{\partial\mathfrak{U}_1}{\partial\mathbb{x}_1},\ \mathcal{E}_{11}^{2}=\frac{\partial\mathfrak{U}_3}{\partial\mathbb{x}_1}, \tag{6a}$$

$$\mathcal{E}_{22}^{0}=\frac{\partial\mathfrak{V}_0}{\partial\mathbb{x}_2},\ \mathcal{E}_{22}^{1}=\frac{\partial\mathfrak{V}_1}{\partial\mathbb{x}_2},\ \mathcal{E}_{22}^{2}=\frac{\partial\mathfrak{V}_3}{\partial\mathbb{x}_2}, \tag{6b}$$

$$\mathcal{E}_{33}^{1}=\mathfrak{W}_1,\ \mathcal{E}_{33}^{2}=\mathfrak{W}_2, \tag{6c}$$

$$\gamma_{12}^{0}=\frac{\partial\mathfrak{U}_0}{\partial\mathbb{x}_2}+\frac{\partial\mathfrak{V}_0}{\partial\mathbb{x}_1},\ \gamma_{12}^{1}=\frac{\partial\mathfrak{U}_1}{\partial\mathbb{x}_2}+\frac{\partial\mathfrak{V}_1}{\partial\mathbb{x}_1},\ \gamma_{12}^{2}=\frac{\partial\mathfrak{U}_3}{\partial\mathbb{x}_2}+\frac{\partial\mathfrak{V}_3}{\partial\mathbb{x}_1}, \tag{6d}$$

$$\gamma_{13}^{0}=\mathfrak{U}_1+\frac{\partial\mathfrak{W}_0}{\partial\mathbb{x}_2},\ \gamma_{13}^{1}=2\mathfrak{U}_2+\frac{\partial\mathfrak{W}_1}{\partial\mathbb{x}_2},\ \gamma_{13}^{2}=\frac{\partial\mathfrak{W}_2}{\partial\mathbb{x}_2}, \tag{6e}$$

$$\gamma_{23}^{0}=\mathfrak{U}_1+\frac{\partial\mathfrak{V}_0}{\partial\mathbb{x}_1},\ \gamma_{23}^{1}=2\mathfrak{U}_2+\frac{\partial\mathfrak{V}_1}{\partial\mathbb{x}_1},\ \gamma_{23}^{2}=\frac{\partial\mathfrak{V}_2}{\partial\mathbb{x}_1}, \tag{6f}$$

4. Constitutive relations

4.1 Constitutive relations

According to Hooke's rule, the stress vector is written as $\sigma^{c}=[\sigma_{11}^{c},\sigma_{22}^{c},\sigma_{33}^{c},\sigma_{12}^{c},\sigma_{13}^{c},\sigma_{23}^{c}]^{T}$, because the constraint of σ_{33}^{c} is zero. The relationship between the stress tensor and strain vector, $\boldsymbol{\mathcal{E}}=[\mathcal{E}_{11},\mathcal{E}_{22},\mathcal{E}_{33},2\mathcal{E}_{12},2\mathcal{E}_{13},2\mathcal{E}_{23}]^{T}$, is as follows:

$$\boldsymbol{\sigma}^{c}=\mathbf{C}^{c}\boldsymbol{\mathcal{E}}, \tag{7}$$

The composite material's elastic constant matrix is denoted by $\mathbf{C}^{c}$.

$$\mathbf{C}^{c}=\begin{bmatrix}\overline{\mathfrak{Q}}_{11}^{c} & \overline{\mathfrak{Q}}_{12}^{c} & \overline{\mathfrak{Q}}_{13}^{c} & 0 & 0 & 0\\ \overline{\mathfrak{Q}}_{12}^{c} & \overline{\mathfrak{Q}}_{22}^{c} & \overline{\mathfrak{Q}}_{23}^{c} & 0 & 0 & 0\\ \overline{\mathfrak{Q}}_{13}^{c} & \overline{\mathfrak{Q}}_{23}^{c} & \overline{\mathfrak{Q}}_{33}^{c} & 0 & 0 & 0\\ 0 & 0 & 0 & \overline{\mathfrak{Q}}_{66}^{c} & 0 & 0\\ 0 & 0 & 0 & 0 & \overline{\mathfrak{Q}}_{44}^{c} & 0\\ 0 & 0 & 0 & 0 & 0 & \overline{\mathfrak{Q}}_{55}^{c}\end{bmatrix}, \tag{8}$$

$$\overline{\mathfrak{Q}}_{11}^{c}=\frac{E_{11}}{\varDelta}(1-\nu_{23}\nu_{32}),\quad \overline{\mathfrak{Q}}_{22}^{c}=\frac{E_{22}}{\varDelta}(1-\nu_{31}\nu_{13}),\ \overline{\mathfrak{Q}}_{33}^{c}=\frac{E_{33}}{\varDelta}(1-\nu_{12}\nu_{21}),$$

$$\overline{\mathfrak{Q}}_{44}^{c}=G_{23},\ \overline{\mathfrak{Q}}_{55}^{c}=G_{13},\ \overline{\mathfrak{Q}}_{66}^{c}=G_{12},\ \overline{\mathfrak{Q}}_{12}^{c}=\frac{E_{11}}{\varDelta}(\nu_{21}+\nu_{31}\nu_{23}),$$

$$\overline{\mathfrak{Q}}_{13}^{c}=\frac{E_{11}}{\varDelta}(\nu_{31}+\nu_{21}\nu_{32}),\ \overline{\mathfrak{Q}}_{23}^{c}=\frac{E_{22}}{\varDelta}(\nu_{32}+\nu_{12}\nu_{31}),$$

$$\varDelta=1-\nu_{12}\nu_{21}-\nu_{23}\nu_{32}-\nu_{31}\nu_{13}-2\nu_{12}\nu_{32}\nu_{13}.$$

Hamilton's principle, which is extended in the following way for the scenario being studied, is used to generate the governing equations (Reddy 2003):

$$\int_0^t (\delta\mathbb{u} - (\delta T + \delta W_1))\, \mathrm{d}t = 0, \tag{9}$$

where t stands for any random moment in time. The following formula is used to calculate the sandwich plate's variations in strain energy ($\delta\mathbb{u}$) and kinetic energy (δT):

$$\delta\mathbb{u} = \int_0^b \int_0^a \int_{-0.5h}^{0.5h} \{\sigma_{11}\delta\mathcal{E}_{11} + \sigma_{22}\delta\mathcal{E}_{22} + \sigma_{33}\delta\mathcal{E}_{33} + 2\sigma_{12}\delta\mathcal{E}_{12} + 2\sigma_{23}\delta\mathcal{E}_{23} + 2\sigma_{13}\delta\mathcal{E}_{13}\}\mathrm{d}\mathbb{x}_3\mathrm{d}\mathbb{x}_1\mathrm{d}\mathbb{x}_2, \tag{10a}$$

$$\delta T = \int_0^b \int_0^a \int_{-0.5h}^{0.5h} \left\{\rho^{(k)}\{\dot{\mathbb{u}}_1[\delta\dot{\mathfrak{U}}_0 + \mathbb{x}_3\delta\dot{\mathfrak{U}}_1 + \mathbb{x}_3^3\delta\dot{\mathfrak{U}}_3] + \dot{\mathbb{u}}_2[\delta\dot{\mathfrak{V}}_0 + \mathbb{x}_3\delta\dot{\mathfrak{V}}_1 + \mathbb{x}_3^3\delta\dot{\mathfrak{V}}_3] + \dot{\mathbb{u}}_3[\delta\dot{\mathfrak{W}}_0 + \mathbb{x}_3\delta\dot{\mathfrak{W}}_1 + \mathbb{x}_3^2\delta\dot{\mathfrak{W}}_2]\}\right\} \mathrm{d}\mathbb{x}_3\mathrm{d}\mathbb{x}_1\mathrm{d}\mathbb{x}_2, \tag{10b}$$

Additionally, the following formula would be used to calculate the variance in work performed by the elastic substrate:

$$\delta W_1 = \int_A \left(-K_w\mathbb{u}_3 + K_p\nabla^2\mathbb{u}_3\right)\delta\mathbb{u}_3 dA \tag{11}$$

The symbols K_w, and K_p stand for the foundation's Winkler coefficient and Pasternak coefficient, respectively.

5. PINNs solution procedure

A deep learning architecture called Physics-Informed Neural Networks (PINNs) integrates physical rules, represented as partial differential equations (PDEs), directly into neural network training. PINNs use automated differentiation to impose starting conditions, boundary conditions, and governing equations as soft restrictions in the loss function rather than depending just on data. PINNs are mesh-free and very convenient for complex geometries, as there is no need for a grid, like typical numerical methods such as the finite element method. PINNs offer an integrated solution for solving nonlinear, interconnected electromechanical systems and learning unknown parameters simultaneously by embedding the physics into the neural network. They are a powerful method for scientific computing and engineering applications because they can also handle inverse problems and parameter identification. The following steps are considered when using the PINN approach to solve governing equations:

5.1 Replace Legendre Polynomial Expansions with Neural Networks (NNs)

We use deep neural networks to estimate the displacement and electric potential fields rather than Legendre polynomial expansions (Eqs. 12a-12j):

$$\mathfrak{U}_0(\mathbb{x}_1, \mathbb{x}_2, t) = N_{\mathfrak{U}_0}(\mathbb{x}_1, \mathbb{x}_2, t, \theta), \tag{12a}$$

$$\mathfrak{V}_0(\mathbb{x}_1, \mathbb{x}_2, t) = N_{\mathfrak{V}_0}(\mathbb{x}_1, \mathbb{x}_2, t, \theta), \tag{12b}$$

$$\mathfrak{W}_0(\mathbb{x}_1, \mathbb{x}_2, t) = N_{\mathfrak{W}_0}(\mathbb{x}_1, \mathbb{x}_2, t, \theta), \tag{12c}$$

$$\mathfrak{U}_1(\mathbb{x}_1, \mathbb{x}_2, t) = N_{\mathfrak{U}_1}(\mathbb{x}_1, \mathbb{x}_2, t, \theta), \tag{12d}$$

$$\mathfrak{V}_1(\mathbb{x}_1, \mathbb{x}_2, t) = N_{\mathfrak{V}_1}(\mathbb{x}_1, \mathbb{x}_2, t, \theta), \tag{12e}$$

$$\mathfrak{W}_1(\mathbb{x}_1, \mathbb{x}_2, t) = N_{\mathfrak{W}_1}(\mathbb{x}_1, \mathbb{x}_2, t, \theta), \tag{12f}$$

$$\mathfrak{U}_3(\mathbb{x}_1, \mathbb{x}_2, t) = N_{\mathfrak{U}_3}(\mathbb{x}_1, \mathbb{x}_2, t, \theta), \tag{12g}$$

$$\mathfrak{V}_3(\mathbb{x}_1, \mathbb{x}_2, t) = N_{\mathfrak{V}_3}(\mathbb{x}_1, \mathbb{x}_2, t, \theta), \tag{12h}$$

$$\mathfrak{W}_2(\mathbb{x}_1, \mathbb{x}_2, t) = N_{\mathfrak{W}_2}(\mathbb{x}_1, \mathbb{x}_2, t, \theta), \tag{12i}$$

$$\psi_a(\mathbb{x}_1, \mathbb{x}_2, t) = N_{\psi_a}(\mathbb{x}_1, \mathbb{x}_2, t, \theta), \tag{12j}$$

$$\psi_s(\mathbb{x}_1, \mathbb{x}_2, t) = N_{\psi_s}(\mathbb{x}_1, \mathbb{x}_2, t, \theta). \tag{12k}$$

where θ stands for the neural networks' trainable weights and biases. A deep neural network with inputs $(\mathbb{x}_1, \mathbb{x}_2, t)$ is represented by each N.

5.2 Boundary and initial conditions

The loss function is represented using boundary and beginning conditions:
- Clamped BCs:

$$L_{BC} = \sum \left|\left|\mathfrak{U}_0(\partial\Omega, t)\right|\right|^2 + \left|\left|\nabla\mathfrak{U}_0(\partial\Omega, t)\right|\right|^2 + \ldots.. \tag{13}$$

- Initial Conditions:

$$L_{IC} = \sum |\mathfrak{U}_0(\mathbb{x}_1, \mathbb{x}_2, 0) - \mathfrak{U}_0^{data}||^2 + ||\dot{\mathfrak{U}}_0(\mathbb{x}_1, \mathbb{x}_2, 0) - \dot{\mathfrak{U}}_0^{data}||^2 + \ldots.. \tag{14}$$

5.3 Governing PDE Residuals

As residuals, the electromechanical PDEs are enforced:
- Mechanical Residual: $R_m = m\,\ddot{u} + C\,\dot{u} + Ku - f$
- Electrical Residual (Maxwell's Equations): $Re = \nabla \cdot D - q = 0$

Total PDE loss: $L_{PDE} = \sum ||Rm||^2 + ||Re||^2$

5.4 Damping and stiffness modifications

Including modified stiffness and Rayleigh damping:
- Damping Term: $C = \alpha R_m + \beta R_k u + G_v\left[k_{\psi u}\right]_a\left[k_{\psi\psi}^{-1}\right]_s\left[k_{\psi u}\right]_s$
- Stiffness Term: $K = k_{uu} + G_d[k_{\psi u}]_a[k_{\psi\psi}^{-1}]_s[k_{\psi u}]_s$

5.5 Training loss function

The total loss function:

$$L_{total} = \lambda_{PDE} L_{PDE} + \lambda_{BC}L_{BC} + \lambda_{IC}L_{IC} + \lambda_{\psi_s}L_{\psi_s} + \lambda_{\psi_a}L_{\psi_a} + \lambda_{charge}L_{charge} \tag{15}$$

where λ terms are weighting hyperparameters.

5.6 Rayleigh damping coefficients

The coefficients α_R and β_R are treated as trainable parameters: α_R, $\beta_R \leftarrow$ learned via gradient descent to minimize L_{total}.

5.7 Implementation Steps

1. Define neural network architectures for all field variables.
2. Sample collocation points in (X_1, X_2, t) space.
3. Compute derivatives using automatic differentiation.
4. Construct loss terms for PDEs, BCs, ICs, and control relations.
5. Train the NNs by minimizing L_{total} using a gradient-based optimizer.

Furthermore, the dimensionless parameters may be expressed as follows:

$$K_W^* = \frac{K_w a^4}{E_m I},\ K_P^* = \frac{K_p a^2}{E_m I},\ \omega^* = \omega a \sqrt{\frac{\rho_m}{E_m}} \tag{16}$$

6. Results and discussion

6.1 Verification study

Table 2 includes a comparison between the reference work of Ref. (Song *et al*. 2017) and the current study investigating the natural frequencies of composite structures having different distributions of reinforcements. Three reinforcement distribution patterns of graphene platelets (GPLs) were considered for the analysis: uniformly distributed (GPL-UD), functionally oriented (GPL-O), and cross-oriented (GPL-X), based on pure epoxy. For all vibration modes (1, 1), (2, 1), and (2, 2) examined, the current results were in close agreement with the reference, showing differences that were negligible in all configurations. This not only validates the robustness of the current modeling and solution approach but also suggests that, from a material standpoint, GPLs greatly improve the natural frequencies over pure epoxy and GPL-X, showing the most improvement, followed by GPL-UD and GPL-O. These improvements appear to substantiate the significant role of reinforcement orientation in governing dynamic stability. In the context of ongoing research on Cu-Ni carbon composite structures based on PINNs, this table highlights the significance of rigour in multiscale material modelling and dynamics prediction. Similarly, to GPL composites with frequency response being dictated by the reinforcement orientation, multiscale surely augmented a PINN's capacity to improve the stability limits (or bounded behaviors) and vibration dynamics of the composite Cu-Ni-carbon system. In summary, the convergence between the reference and the current findings accentuates the strength of implementing higher-order theories and machine learning solutions in accounting for and managing the dynamic stability of multifunctional composites.

6.2 Parametric results

The relative frequency change (RFC) has been used in this study to illustrate how the frequency is dependent on the applied voltage.

Table 2 A comparative study between the reference work of Ref. (Song *et al.* 2017) and the present investigation, focusing on the natural frequencies of composite structures with different reinforcement distributions

Mode number		Pure epoxy	GPL-UD	GPL-O	GPL-X
(1, 1)	Ref. (Song *et al.* 2017)	0.0584	0.1216	0.1020	0.1378
	Present	0.0582	0.1214	0.1019	0.1377
(2, 1)	Ref. (Song *et al.* 2017)	0.1391	0.2895	0.2456	0.3249
	Present	0.1389	0.2893	0.2454	0.3247
(2, 2)	Ref. (Song *et al.* 2017)	0.2132	0.4436	0.3796	0.4939
	Present	0.2131	0.4434	0.3794	0.4937

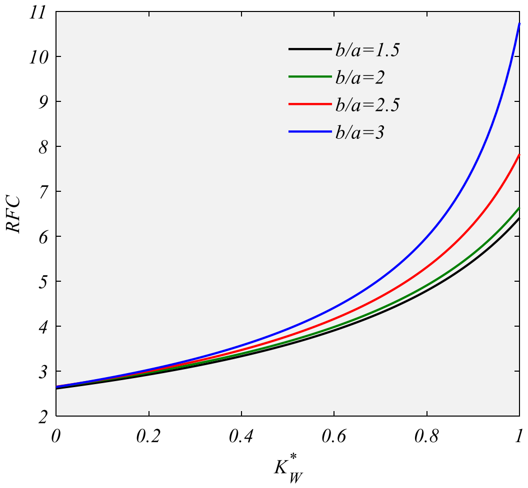

Fig. 2 The influences of K_W^* and b/a ratio on the RFC of the presented composite structure.

$$\omega_{RF} = |\omega_1 - \omega_2|/\omega_2. \tag{17}$$

The present smart structure's natural frequency with and without applied voltage is shown by ω_1, and ω_2, respectively.

Fig. 2 shows how the change in relative frequency (RFC) depended upon the dimensionless Winkler foundation modulus, K_W^*, for a range of aspect ratios. In summary, RFC increased as K_W^* increased, which indicates that the elastic foundation stiffness was an important factor in increasing dynamic stability; this was more pronounced at the larger values of K_W^* and a non-linear increase was observed as well. Moreover, when comparing different aspect ratios, the plates with larger b/a had larger values of RFC, which indicates that RFC was more dependent upon the foundation stiffness in these plates; for example, the configuration b/a=3 had the steepest increase compared with just a modest increase in RFC for b/a=1.5. This trend also indicates that the longer structure was more sensitive to the support provided by the substructure, as increased flexibility, along the longer span, can increase its response to support. The results evident from the top-left figure must be taken into account, especially while training any critical buckling or vibrating behaviors at varying aspect ratios as geometric scaling effects emerge and implications for material management

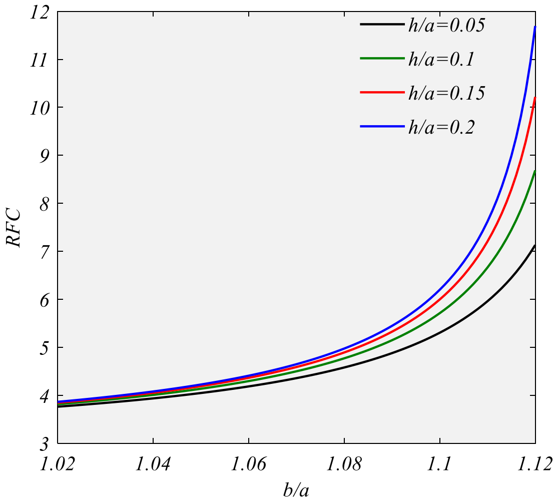

Fig. 3 The influences of h/a and b/a ratio on the RFC of the presented composite structure

practices indicate that modifying and/or selecting the appropriate aspect ratio of a composite in conjunction with a modicum of a particular foundation module is worth considering as a more suitable stabilization approach. Overall, the first figure confirms that there is more potential to enhance vibration performance from modifying Winkler stiffness, which can be implemented with the structural geometry of Cu–Ni carbon composites.

Fig. 3 shows how the relative frequency change varies with the aspect ratio for various normalized thickness ratios. For all the thickness ratios, in this analysis, we see RFC exhibiting a steep and nonlinear increase with b/a indicating the critical nature of structural slenderness for stability improvement, and thicker plates (higher h/a) consistently present improved stability through increased RFC values because of improved cross-section stiffness. For the h/a=0.2 case, we see a steepest increase where RFC approaches RFC values of nearly 12 at the upper limit b/a. This trend indicates the thicker Cu–Ni carbon composites transferring the load more effectively while working through the elastic constraints posed by the substructure during the natural frequencies shift. The consistent ordering among the curves suggests there is a close relationship between the thickness ratio and how quickly the plate reacts, while being independent of the actual geometry of the plate. In our proposed PINN system, we incorporate higher-order shear deformation theory, which ensures that thickness-dependent responses will happen without the need for shear correction factors. We see the important connection of thickness ratios and loads being managed geometrically and material scales together to predictively model system behavior that is in alignment with experimental features. Thus, engineers can actively manage a frequency-dependent stability aspect of the composite through selecting appropriate h/ah/ah/a values during fabrication.

Fig. 4 shows the development in the relative frequency change (RFC) response with aspect ratio at different dimensionless values for Pasternak foundation moduli (K_P^*). In all instances, RFC shows a sharp decrease with increasing b/a, where RFC settles at a baseline or lower bound for higher aspect ratios. Crucially, a higher value of K_P^* produced a higher RFC, showing that the moduli of the Pasternak shear layer enhance frequency management. For example, the K_P^*=0.3 condition had the highest RFC values across the board, while K_P^*=0 ended with the smallest response. The activity

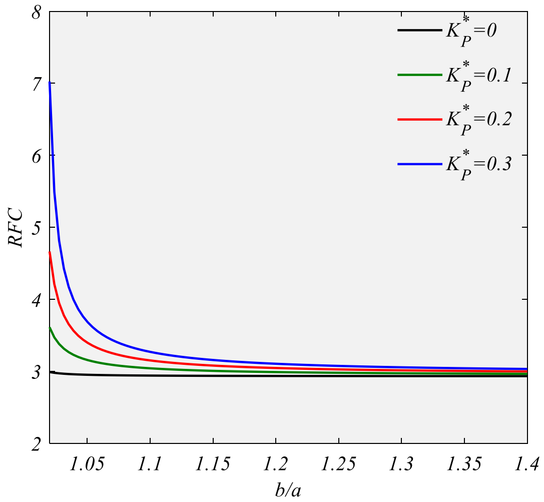

Fig. 4 The influences of K_P^* and b/a ratio on the RFC of the presented composite structure

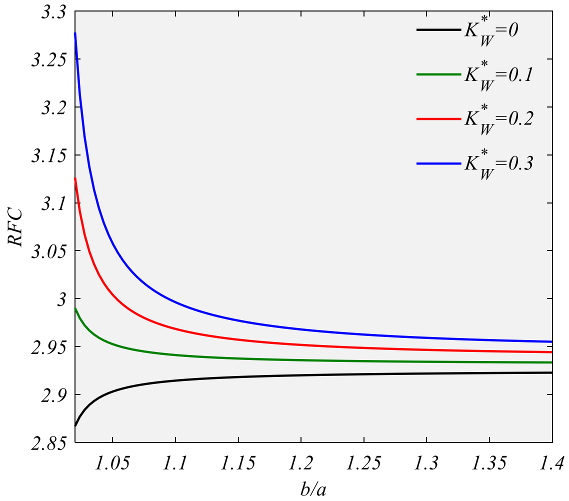

Fig. 5 The influences of K_W^* and b/a ratio on the RFC of the presented composite structure

of the Pasternak foundation is significant because it adds additional shear interactions that depart from Winkler due to stress laterally redistributing. The diminishing sensitivity at higher b/a ratios tells us explicitly that larger and more elongated geometries are less susceptible to systemic foundation shear influence, while near-square geometries are more sensitive to shear. To this end, from a machine-learning standpoint, the noted interactions with respect to K_P^* and geometry should signal PINNs to develop their coupled geometric-foundation effects when predicting dynamic response. The larger implications for engineering management of Cu–Ni carbon composites are that when seeking to optimize vibrational performance, it is important to instructor calibration of the aspect ratio and shear foundation stiffness.

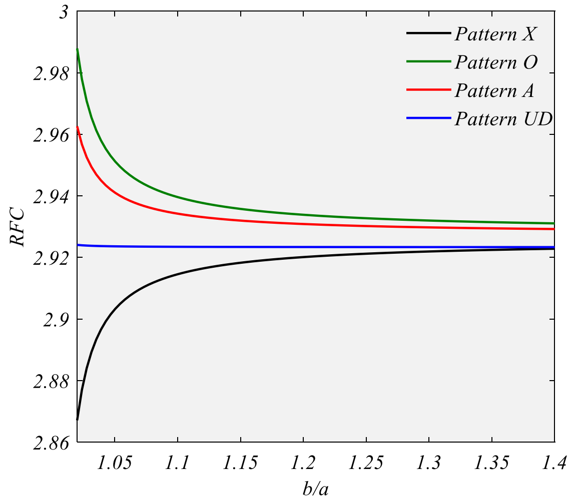

Fig. 6 A comparison of the relative frequency change based on aspect ratio for four distinct reinforcement patterns

Fig. 5 illustrates the effect of the dimensionless Winkler modulus on the normalized frequency change with respect to aspect ratio, and while in contrast to previous monotonic tendencies, RFC displays a consistent, albeit subtle stabilization mannerism. For all cases, the frequency normalized upon the stiffness factor shows an abrupt drop at small ratio b/a values, before coming to approximately constant values as aspect ratios become larger. Higher values of K_W^* have an upward shift of the RFC curves with improved Winkler concentration yields greater natural frequency changes even in longer forms. For example, K_W^*=0.3 maintains higher RFC's compared to K_W^*=0, even though the relative impact becomes less as b/a becomes skewed. The implication is that stiffness effects of the foundation from modally contributing elements all reside primarily in the quantifiable value of a nearly square plate, while longer and longer structures rely on the geometric proportion and structural connectome of the building envelope rather than the effects of substructure shown in Winkler contributions. The greatest bearing lay in the close proximity of the curves found from greater b/a which shows the diminished influence felt. Within the PINN modeling strategy, the behavior highlights the necessity for localized features training sensitivity to capture the low-aspect-ratio dominance of foundation effects. Fig. 5 shows us that while Winkler stiffness will always be favorable for changes to building mechanics, the factor of proportion of which substructure management is an impactful mechanism for structural performance will be bipolar to the physical part geometry or shape. With dynamic stability concerns, we are left pondering the relationship between foundation mechanics and spatial form.

Fig. 6 provides a comparison of the relative frequency change (RFC) based on aspect ratio for four distinct reinforcement patterns. Pattern X, Pattern O, Pattern A, and Pattern UD. For all cases, the RFC decreased as b/a increased and stabilized to almost constant values for elongated geometries. Pattern X had the lowest RFC starting from a base of about 2.87 and minimally increased as the aspect ratio increased, while Pattern O and Pattern A took on higher RFC bases and modest decreasing trends. As the only pattern with fiber orientation remaining virtually unchanged, Pattern UD demonstrated the most stable response, maintaining an RFC at or around 2.92 regardless of aspect ratio. This suggests that unidirectional fiber alignment provides predictable vibrational

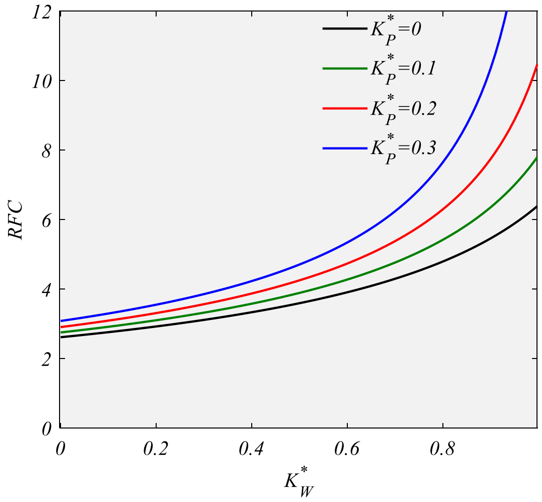

Fig. 7 A comparison of the relative frequency change based on K_W^* for four K_P^* values

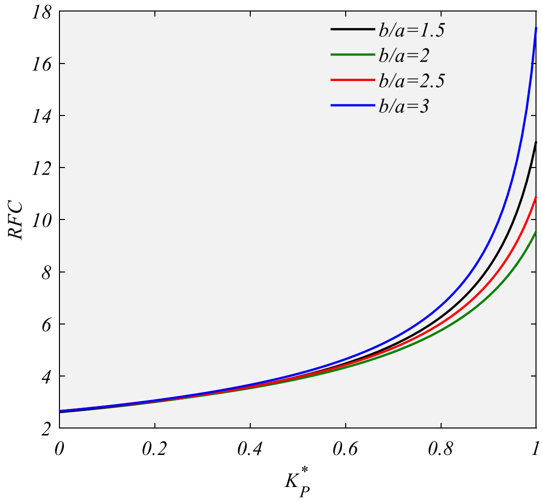

Fig. 8 A comparison of the relative frequency change based on K_W^* for four b/a values

performance, which may be useful, particularly in cases that require a predictable frequency response across varying geometries. The reinforcement schemes that employ cross and angles are proven to have high sensitivity, offering potential for tuning dynamic responses at the expense of an overall more variable response. The overall separation among the curves confirms the importance of fiber orientation in determining substructural interaction within the Cu-Ni matrix and applied within the PINN environment, conveys the importance of encoding fiber patterning effects as independent features for accurate modeling of frequency management strategies within multifunctional composites.

Fig. 7 shows how the relative frequency change varies with dimensionless Winkler modulus under different values of Pasternak foundation stiffness. In all cases considered, RFC is a monotonic

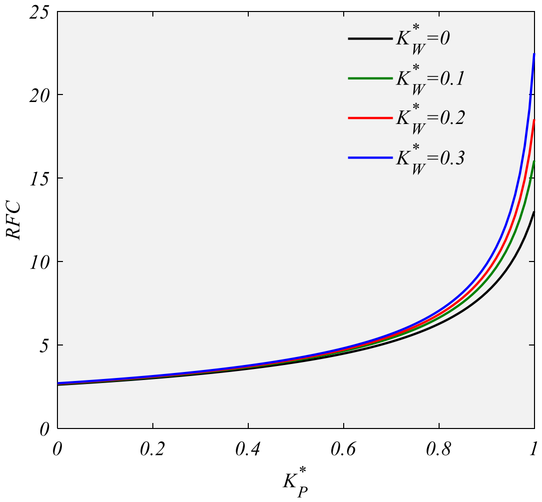

Fig. 9 The relationship of RFC versus dimensionless Pasternak modulus for varying Winkler foundation stiffnesses

function of K_W^* and has an increasing rate of change at higher values of K_W^*, particularly as K_W^* nears 1. The notable effect of K_P^* is evident: at larger values, K_P^* raised the RFC curves significantly more, and anything close to K_W^* just from varying Winkler modulus is impossible to subsequently understand the frequency shift. For instance, for K_W^*=0.8, in the case of K_P^*=0.3 the RFC value was just under 11, while the case of K_P^*=0 remained around 7. A clear relationship between Winkler and Pasternak parameters demonstrates that vertical and shear elastic support acting in unison helps to control the dynamic (or elastic) stability of composite configurations. More importantly, there is a potential for nonlinearity, which suggests that either foundation parameter by itself, without weighting, will yield an underestimate of the dynamic (lateral) stability limits. Turning to modeling based on PINN, these results further emphasize the importance of needing to include both elastic coefficients as governing input simultaneously in order to develop a model that approximates how the observable behaviors of interest were realized in practice. The engineering implications are clear. By varying the stiffness or shear stiffness K_P^* of the foundation generates an increase in the overall stabilizing element of Winkler elasticity that potentially allows for more refined control of vibration responses in carbon composites of Cu-Ni, or whatever properties these composites possess across a range of realistic loading configurations.

From Fig. 8, it is clear that the aspect ratio has an effect, and naturally, the slender geometry (b/a=3) revealed the greatest change in frequency (RFC), and the thicker geometry (b/a=1.5), the least. For example, for K_P^*=1, the RFC is nearly 18 for b/a=3, while for b/a=1.5 it is suspiciously close to 15. This observation provides evidence that slender structures will be the most affected by shear-layer foundation effects because they are ultimately more flexible and capable of redistributing stress. The sharp nonlinear rise at the higher stiffnesses indicates the multiplicative effect of the shear foundation resistance, as less load is being carried by the elastic support, and greater resistance is present to increase the stability of the vibration of the structure. From the perspective of the process of implementing a PINN, it is essential to account for the aspect ratio–foundation coupling in order to make accurate predictions of the frequency changes. From an engineer's perspective on

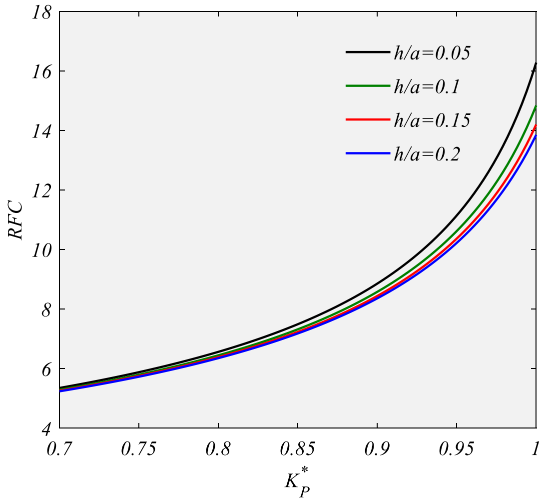

Fig. 10 The relationship between the RFC and normalized Pasternak modulus for plates of varying thickness ratios

choosing a K_P^* value greater than 1, this presents an opportunity to dynamically stabilize slender Cu–Ni composites, in shear-layer foundation interaction, thus enhancing utilization in load-bearing, vibration-suppressing applications.

Fig. 9 shows the relationship of RFC versus dimensionless Pasternak modulus for varying Winkler foundation stiffnesses. Expectedly, RFC monotonically increases with increasing. K_P^*, but the absolute value of this increase seems to be heavily influenced by K_W^*. That is, the higher the values of Winkler stiffness, the higher the RFC curves are laid out; for example, the K_W^*=0.3 case reaches values above 22 at K_P^*=1, while the K_W^*=0 case only achieves about 18, for the same K_P^*. The amplification effect supports the idea of normal (Winkler) and shear (Pasternak) foundation mechanisms working cooperatively to improve vibrational stability. The nonlinear response at high values of K_P^* is suggestive that once the shear layer is stiff enough, there is an additional amplifying effect from Winkler elasticity in increasing the natural frequency shifts. In the PINN approach, this coupling strongly suggests the need to encode foundation parameters as interdependent variables rather than univariate features. From a pragmatic viewpoint, these results demonstrate that optimizing both K_W^* and K_P^* together is the best approach to maximize control over issues of dynamic stability, especially in applications that require maximizing frequency shifts in Cu-Ni carbon composites.

Fig. 10 investigates the relationship between the RFC and normalized Pasternak modulus for plates of varying thickness ratios. In all instances, RFC show a nonlinear increase, dependent on K_P^* approaching 1, illustrating the enhancing effect of shear-layer stiffness on the frequency changes. Notably, at all values of K_P^* we've examined, the thinner plates (h/a=0.05) have larger RFC, than the thicker configurations we analyzed (h/a=0.2). This difference suggests that the slender plates may be more sensitive to shear-layer effects, potentially due to the reduced in-plane rigidity alleviating the constraint variations with the elastic foundation. For example, at K_P^*=1, the thinnest plate has an RFC of around 17 and the thickest plate stabilizes at around 15. The convergence in curves at lower K_P^* implies that thickness impacts are negligible or weakly observable when the shear-layer support is weak, but then become more noteworthy as the shear

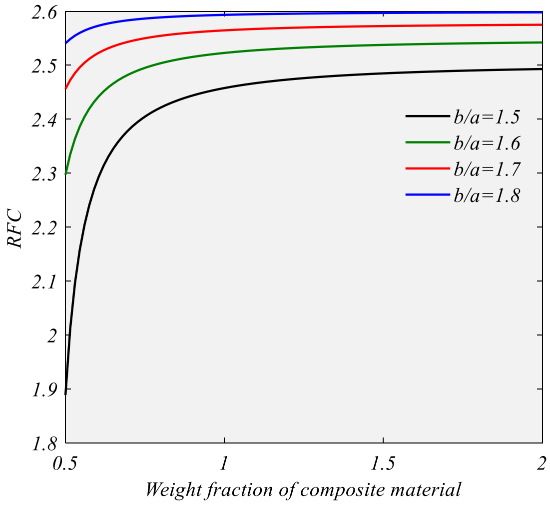

Fig. 11 The dependence of relative frequency change on the weight fraction of composite material with the variable of aspect ratio

foundations modulus increases. Within the paradigm of higher-order shear deformation theory, coupled with PINNs, sensitivity to the thickness contribution should be included for predictive modeling. Viewpoint applied to design, this demonstrates the importance of matching the plate's slenderness along with the shear stiffness of the foundation on achieving a required vibrational performance for Cu–Ni carbon composites.

Fig. 11 illustrates the dependence of relative frequency change on the weight fraction of composite material with the variable of aspect ratio. A distinct monotonic trend can be seen: RFC rises quickly within lower fraction composites, followed by the following saturation once the materials' weight fraction is mostly greater than unity. This is indicative of the non-linear relationship of initial increases in an excellent reinforcement providing significant history of vibrational performance, while further increases only represent a smaller fraction of vibrational performance values, aspect ratio becomes critically relevant with juts above slender objects (b/a=1.8) demonstrating the highest RFC values throughout the entire range of composite incorporation, whereas more stubby shapes (b/a=1.5) have little responses for reinforcement values. For this example, the value of RFC is mostly stabilized at 2.6 with a weight fraction of 2 for b/a=1.8, to approximately 2.5 for b/a=1.5. This indicates that the slenderness of geometry exacerbates the beneficial effects of composite enhancement by augmenting the capacity for load transfer and mutual stiffness of jointly engaging structures through Cu-Ni material. There was a prominent and quick convergence of curves as each aspect of the experiment crossed higher than a value of material reinforcement. This demonstrates that once the material reinforcement crossed over values of significance, it became a small geometric aspect in motion to consider the control effects. Incorporation provides that the relationship guarantees that the sensitivity of frequency prediction in a PINN-based model could be demonstrated visually through performing geometrically varying material reinforcement levels. The engineering relevance of the analysis provides guidance on overall reinforcing ratios for operability through the geometry to promote the best level of stability management.

7. Conclusions

This investigation includes a systematic control of the dynamic stability in Cu-Ni carbon composite structures through an integration of micro mechanical models, advanced structural theory, and data-driven solution processes. Effective elastic and shear properties of the Cu-Ni carbon composite have been meaningfully computed using modified Halpin-Tsai models, producing realistic characterizations of interception mechanisms and interfacial interactions. Realistic elastic properties allowed the governing equations of motion to be derived without neglecting material or structural nonlinearities and using Hooke's rule and Hamilton's principle. An effective higher-order shear deformation theory using three displacement variables provides a richer modeling of transverse shear effects and removes all empirical shear correction factors. The introduction of elastic foundation parameters, which included a Winkler model and Pasternak model, has sufficiently represented subgrade reaction and shear interrelations, where the set solutions have enhanced the theoretical groundworks for an intricate series of subsequent engineering to derive relatively simplified analytical rigor from such physically complex engineering mechanics to actual engineering application. The advent of physics-informed neural networks has floridly provided a generative computational methodology that expresses physical governing laws of motion with machine learning techniques. This methodology has facilitated mesh-free, data-efficient, and higher accurate solutions that substantially reduce the expense of computational utilization than conventional numerical approaches. Accurate predictions of critical parameters such as buckling loads, vibration modes, and stability boundaries were achieved, and the comparisons with finite element results demonstrated the reliability of the proposed framework. Overall, this study has assisted in managing multifunctional composite materials through a blend of theoretical, numerical, and data-centric methods. The results provided a developing understanding of how Cu–Ni carbon composites respond to dynamic loading, which has established for the design and optimization of next-generation smart and multifunctional structures. By converging homogenization techniques, higher-order shear deformation theory, and physics-informed neural networks, this work has created a multitude of opportunities.

Acknowledgment

The research is funded by Zarqa University.

References

Abderezak, R., Rabia, B., Daouadji, T. H., Abbes, B., Belkacem, A. and Abbes, F. (2018), "Elastic analysis of interfacial stresses in prestressed PFGM-RC hybrid beams", *Adv. Mater. Res.*, **7**(1), 83-98. https://doi.org/10.12989/amr.2018.7.1.083

Azmi, M., Kolahchi, R. and Bidgoli, M. R. (2019), "Dynamic analysis of concrete column reinforced with SiO2 nanoparticles subjected to blast load", *Adv. Concr. Constr.*, **7**(1), 51-62. https://doi.org/10.12989/acc.2019.7.1.051

Carrera, E. (1996), "C0 Reissner-Mindlin multilayered plate elements including zig-zag and interlaminar stress continuity", *Int. J. Numer. Meth. Eng.* **39**(11), 1797-1820. https://doi.org/10.1002/(SICI)1097-0207(19960615)39:11<1797::AID-NME935>3.0.CO;2-0

Carrera, E. (2001), "Developments, ideas, and evaluations based upon Reissner's Mixed Variational Theorem in the modeling of multilayered plates and shells", *Appl. Mech. Rev.*, **54**(4), 301-329. https://doi.org/10.1115/1.1385512

Duc, L.B., Le, B.T., Quoc, K.D., Tran, T.B. and Singh, R. (2025), "Investigation the effects of compaction pressure and sintering temperature on mechanical properties of Al-x% TiC composite", *Adv. Mater. Res.*, **14**(1), 71-79. https://doi.org/10.12989/amr.2025.14.1.071

Ebrahimi, F., Dehghan, M. and Seyfi, A. (2019), "Eringen's nonlocal elasticity theory for wave propagation analysis of magneto-electro-elastic nanotubes", *Adv. Nano Res.*, **7**(1), 1-11. https://doi.org/10.12989/anr.2019.7.1.001

Eshaghi, M. S., Anitescu, C., Thombre, M., Wang, Y., Zhuang, X. and Rabczuk, T. (2025), "Variational physics-informed neural operator (vino) for solving partial differential equations", *Comput. Meth. Appl. Mech. Eng.*, **437**, 117785. https://doi.org/10.1016/j.cma.2025.117785

Garg, A., Belarbi, M.O., Li, L., Chalak, H., Tounsi, A. and Zenkour, A. (2024), "Comparative study on the buckling analysis of exponential, power and sigmoidal sandwich FGM plates under hygro-thermal conditions", *Adv. Mater. Res.*, **13**(5), 431-462. https://doi.org/10.12989/amr.2024.13.5.431

Guo, H., Zhuang, X., Alajlan, N. and Rabczuk, T. (2023), "Physics-informed deep learning for melting heat transfer analysis with model-based transfer learning", *Comput. Math. Appl.*, **143**, 303-317. https://doi.org/10.1016/j.camwa.2023.05.004

Guo, H., Zhang, C., Fang, H., Rabczuk, T. and Zhuang, X. (2025), "Deep learning to evaluate seismic-induced soil liquefaction and modified transfer learning between various data sources", *Undergr. Space.*, **23**, 220-242. https://doi.org/10.1016/j.undsp.2024.02.001

Hajmohammad, M.H., Zarei, M.S., Farrokhian, A. and Kolahchi, R. (2018), "A layerwise theory for buckling analysis of truncated conical shells reinforced by CNTs and carbon fibers integrated with piezoelectric layers in hygrothermal environment", *Adv. Nano Res.*, **6**(4), 299-321. https://doi.org/10.12989/anr.2018.6.4.299

Jayakumari, B.Y., Swaminathan, E.N. and Partheeban, P. (2024), "Sustainable construction material using nanosilica and multi-walled carbon nanotubes in cement concrete", *Adv. Nano Res.*, **16**(5), 459-472. https://doi.org/10.12989/anr.2024.16.5.459

Liu, B., Wang, Y., Rabczuk, T., Olofsson, T. and Lu, W. (2024), "Multi-scale modeling in thermal conductivity of Polyurethane incorporated with Phase Change Materials using Physics-Informed Neural Networks", *Renew. Energy*, **220**, 119565. https://doi.org/10.1016/j.renene.2023.119565

Liu, Y., Su, J., Wang, Z., He, D., Wang, T. and Huang, Q. (2025), "Analytical model of flat rolling force for corrugated composite sheet", *Int. J. Mech. Sci.*, 110327. https://doi.org/10.1016/j.ijmecsci.2025.110327

Luo, Y., Zhang, X., Zhou, H. and Elmaimouni, L. (2025), "Shear horizontal wave propagation in piezoelectric semiconductor nanoplates with the consideration of surface effects and nonlocal effects", *Mech. Adv. Mater. Struct.*, 1-17. https://doi.org/10.1080/15376494.2025.2345678

Madenci, E., Ozkilic, Y.O., Hakamy, A. and Tounsi, A. (2023), "Experimental tensile test and micro-mechanic investigation on carbon nanotube reinforced carbon fiber composite beams", *Adv. Nano Res.*, **14**(5), 443-450. https://doi.org/10.12989/anr.2023.14.5.443

Rabczuk, T. and Belytschko, T. (2004), "Cracking particles: A simplified meshfree method for arbitrary evolving cracks", *Int. J. Numer. Meth. Eng.*, **61**(13), 2316-2343. https://doi.org/10.1002/nme.1151

Rahimi, A., Alibeigloo, A. and Safarpour, M. (2020), "Three-dimensional static and free vibration analysis of graphene platelet-reinforced porous composite cylindrical shell", *J. Vib. Control*, **26**(17-18), 1627-1645. https://doi.org/10.1177/1077546320916265

Rashvand, K., Alibeigloo, A. and Safarpour, M. (2022), "Free vibration and instability analysis of a viscoelastic micro-shell conveying viscous fluid based on modified couple stress theory in thermal environment", *Mech. Based Des. Struct.*, **50**(4), 1198-1236. https://doi.org/10.1080/15397734.2020.1760882

Reddy, J.N. (2003). *Mechanics of Laminated Composite Plates and Shells: Theory and Analysis*, CRC Press. https://doi.org/10.1201/9780203911164

Safarpour, M., Rahimi, A., Alibeigloo, A., Bisheh, H. and Forooghi, A. (2021), "Parametric study of three-dimensional bending and frequency of FG-GPLRC porous circular and annular plates on different boundary conditions", *Mech. Based Des. Struct.*, **49**(5), 707-737. https://doi.org/10.1080/15397734.2020.1719509

Samaniego, E., Anitescu, C., Goswami, S., Nguyen-Thanh, V. M., Guo, H., Hamdia, K., Zhuang, X. and Rabczuk, T. (2020), "An energy approach to the solution of partial differential equations in computational mechanics via machine learning: Concepts, implementation and applications", *Comput. Meth. Appl. Mech. Eng.*, **362**, 112790. https://doi.org/10.1016/j.cma.2019.112790

Song, M., Kitipornchai, S. and Yang, J. (2017), "Free and forced vibrations of functionally graded polymer composite plates reinforced with graphene nanoplatelets", *Compos. Struct.*, **159**, 579-588. https://doi.org/10.1016/j.compstruct.2016.09.070

Talebi, H., Silani, M., Bordas, S.P., Kerfriden, P. and Rabczuk, T. (2014), "A computational library for multiscale modeling of material failure", *Comput. Mech.*, **53**(5), 1047-1071. https://doi.org/10.1007/s00466-013-0951-7

Tyona, M. (2013), "A theoretical study on spin coating technique", *Adv. Mater. Res.*, **2**(4), 195-208. https://doi.org/10.12989/amr.2013.2.4.195

Wang, G., Wei, Y., Zhang, X. and Rahimi, A. (2024), "Dynamic stability examination of perovskite solar cells: Application of numerical analysis, GAN and African vulture optimization algorithms", *Aerosp. Sci. Tech.*, **144**, 108736. https://doi.org/10.1016/j.ast.2023.108736

Zerrouki, R., Karas, A. and Zidour, M. (2020), "Critical buckling analyses of nonlinear FG-CNT reinforced nano-composite beam", *Adv. Nano Res.*, **9**(3), 211-220. https://doi.org/10.12989/anr.2020.9.3.211

Zhai, Y., Li, S. and Zhang, X. (2025), "Vibration performance of composite doubly curved shells embedded with damping layer", *Int. J. Struct. Stabil. Dyn.*, 2650265. https://doi.org/10.1142/S0219455426502652

Zhang, G., Xiao, C., Rahimi, A. and Safarpour, M. (2020), "Thermal and mechanical buckling and vibration analysis of FG-GPLRC annular plate using higher order shear deformation theory and generalized differential quadrature method", *Int. J. Appl. Mech.*, **12**(5), 2050019. https://doi.org/10.1142/S1758825120500191

Zouatnia, N. and Hadji, L. (2019), "Static and free vibration behavior of functionally graded sandwich plates using a simple higher order shear deformation theory", *Adv. Mater. Res.*, **8**(4), 313-335. https://doi.org/10.12989/amr.2019.8.4.313

CC